

 Very Important Paper

Nickel-Loaded γ -Alumina Composites for a Radiofrequency-Heated, Low-Temperature CO₂ Methanation Scheme

Wei Wang,^[a] Cuong Duong-Viet,^[a] Giulia Tuci,^[b] Yuefeng Liu,^{*,[c]} Andrea Rossin,^[b] Lapo Luconi,^[b] Jean-Mario Nhut,^[a] Lam Nguyen-Dinh,^[d] Giuliano Giambastiani,^{*,[a, b, e]} and Cuong Pham-Huu^{*,[a]}

In this work, we joined highly Ni-loaded γ -Al₂O₃ composites, straightforwardly prepared by impregnation methods, with an induction heating setup suited to control, almost in real-time, any temperature swing at the catalyst sites (i.e., “hot spots” ignition) caused by an exothermic reaction at the heart of the power-to-gas (P2G) chain: CO₂ methanation. We have shown how the combination of a poor thermal conductor (γ -Al₂O₃) as support for large and highly interconnected nickel aggregates together with a fast heat control of the temperature at the catalytic bed allow part of the extra-heat generated by the reaction exothermicity to be reused for maintaining the catalyst under virtual isothermal conditions, hence reducing the reactor

power supply. Most importantly, a highly efficient methanation scheme for substitute natural gas (SNG) production (X_{CO_2} up 98% with $>99\%$ S_{CH_4}) under operative temperatures (150–230 °C) much lower than those commonly required with traditional heating setup has been proposed. As for as sustainable and environmental issues are concerned, this approach re-evaluates industrially attractive composites (and their large-scale preparation methods) for application to key processes at the heart of P2G chain while providing robust catalysts for which risks associated to nano-objects leaching phenomena are markedly reduced if not definitively suppressed.

1. Introduction

The worldwide consumption of fossil fuels linked to anthropogenic activities produces an uncontrollable increase of CO₂ concentration in the atmosphere. As a matter of fact, global climate change and environmental impact caused by an uncontrolled C-footprint growing are becoming urgent challenges that our modern society must face with. To this aim, renewable energies (REs) are gaining great importance because

they can boost a real transition towards technically and economically feasible decarbonization strategies as to meet the ambitious European Commission objective for a reduction of 80–95% greenhouse gas emissions by 2050.^[1] Nonetheless, carbon-neutral solutions - alternative to current industrial technologies - remain scarce and costly; large efforts are still necessary to overcome limits related to the decentralized and intermittent nature of RE supplies and safety issues^[2] related to their distribution in the existing energy grids.^[3] The development of integrated chemical strategies for energy conversion and storage such as the power-to-gas (P2G) chain is a concrete step forward in the direction of a truly renewable energy-based future.^[4] In P2G technology, surplus of electricity from RE and CO₂-free energy suppliers (i.e., wind, hydraulic, solar) is converted into H₂ via water electrolysis. H₂ can be reacted in turn with CO₂ to give methane (CH₄) as substitute natural gas (SNG) via methanation reaction (Sabatier process).^[5] The as-obtained methane as carbon-neutral fuel may be employed in different practical contexts: redistribution in the existing gas infrastructures, chemical storage of RE, use as reagent in industrial chemical processes or as an energy vector for power generation both in industrial and private sectors.^[4,5b,6]

Although CO₂ methanation is a thermodynamically favorable transformation ($\Delta G^0 = -114 \text{ kJ mol}^{-1}$), it suffers from severe kinetic limitations because of the high CO₂ chemical inertness.^[7] Thus, metal-based catalysts and medium operating temperatures (typically between 300 and 450 °C) are required to run the process efficiently. Too high operating temperatures are generally not recommended because of thermodynamic limitations that lead to a significant decrease of CO₂ conversion, besides affecting the catalyst lifetime. On the other hand, methanation is a highly exothermic reaction ($\Delta H^0 = -$


[a] Dr. W. Wang, Dr. C. Duong-Viet, Dr. J.-M. Nhut, Dr. G. Giambastiani, Dr. C. Pham-Huu
 Institut de Chimie et Procédés pour l’Energie, l’Environnement et la Santé (ICPEES)
 UMR 7515 CNRS- University of Strasbourg (UdS)
 25, rue Becquerel, 67087 Strasbourg Cedex 02 (France)
 E-mail: giambastiani@unistra.fr
 cuong.pham-huu@unistra.fr

[b] Dr. G. Tuci, Dr. A. Rossin, Dr. L. Luconi, Dr. G. Giambastiani
 Institute of Chemistry of OrganoMetallic Compounds, ICCOM-CNR and Consorzio INSTM
 Via Madonna del Piano, 10-50019, Sesto F.no, Florence (Italy)
 E-mail: giuliano.giambastiani@iccom.cnr.it

[c] Prof. Y. Liu
 Dalian National Laboratory for Clean Energy (DNL), Dalian Institute of Chemical Physics
 Chinese Academy of Science
 457 Zhongshan Road, 116023 Dalian (P. R. China)
 E-mail: yuefeng.liu@dicp.ac.cn

[d] Prof. L. Nguyen-Dinh
 The University of Da-Nang
 University of Science and Technology
 54, Nguyen Luong Bang, Da-Nang (Vietnam)

[e] Dr. G. Giambastiani
 Kazan Federal University
 420008 Kazan (Russian Federation)

 Supporting information for this article is available on the WWW under <https://doi.org/10.1002/cssc.202001885>

165 kJ mol⁻¹) responsible for the generation of local temperature gradients (hot spots). Hot spots do not simply impact (detrimentally) on the catalyst performance and its long-term stability on stream but they often pose serious security issues in packed-bed large scale reactors. Hence, costly and energy consuming solutions to remove the heat surplus are required for classical methanation schemes. To date, great efforts have been devoted to the development of efficient and selective catalysts for the process (including engineered core-shell systems featured by excellent performance when operating under less conventional heating schemes)^[8] whereas much less attention has been paid towards energy-saving solutions based on a more effective heat management and temperature control within the reactor. Adiabatic fixed-bed reactors, fluidized-bed or structured three-phase reactors have been used to handle the excess of local heat produced by the reaction exothermicity as to limit its negative impact on the catalyst performance and its stability on run.^[9] Similarly, microstructured catalysts^[10] based on thermally conductive (metallic^[11] or non-metallic^[12]) supports and featured by enhanced heat/mass transfer properties have provided valuable solutions to an efficient control/dissipation of the exceeding heat generated at the catalytic bed.^[13]

Recent progresses in the field of radiofrequency (RF) heated (or inductively heated, IH) catalytic processes have spotlighted on the unique potentiality of this “non-contact” technology for the heat management in highly exo- and endothermic reactions.^[8b] The ability of IH to deliver heat directly where it is needed by means of magnetic or electrically conductive targets (susceptors) with minor energy losses towards catalyst’s surrounding,^[14] has overcome several transfer limitations of classical heating schemes (contact heaters). The almost instantaneous “on/off switching” of the heat supplied at the catalytic bed and the much faster heating/cooling rates of the catalyst active phase (compared to those achievable within more classical heating schemes), allow IH to control the ignition of potentially harmful “hot spots”. Consequently, energy wastes are reduced and catalysts can operate under virtually isothermal conditions, with an improved lifecycle.^[8b] Some of these key-features have recently been exploited with success in CO₂ methanation using magnetic nanoparticles (NPs) with high heating power^[8a,15] including NPs-decorated electrically conductive susceptors operating under severe and dynamic conditions.^[12a] From an engineering viewpoint, several applications have recently contributed to strengthen the IH technology in related areas of sustainable catalysis. Rebrov and co-workers proposed a RF-heated scheme to accomplish in a highly efficient and energy saving manner CO₂ adsorption-desorption cycles on a CaO-based sorbent.^[16] The same team also showed how a multi zone RF-heated reactor can be straightforwardly conceived and realized in order to perform consecutive catalytic processes, each under optimal reaction conditions and continuous operation mode.^[17]

To date, a very large combination of late-transition metals (including those of Pt-group) supported on metal(s)-oxides, silica, carbons or zeolites have been systematically scrutinized while searching for the optimal catalyst for the process.^[6b,18] In spite of that, catalytic materials prepared from cheap and

commercially available components, selected (preferentially) among non-critical raw materials and prepared through easy and costless industrial synthetic strategies, are mandatory features for the development of any sustainable catalytic technology. Accordingly, nickel (as active phase) and Al₂O₃ (as support) remain the preferred choice for the methanation reaction also considering the distinct catalytic properties of the former and the use of the latter as support across many industrially relevant heterogeneous transformations.

Literature lists a high number of reports on the synthesis of Ni@Al₂O₃ catalysts for CO_x (x = 1, 2) methanation. Only a few studies though have been focused on highly nickel-loaded Al₂O₃-based catalysts, because poorly metal dispersed systems featured by oversized (and undesired) Ni particles are typically formed.^[19] Despite several attempts to correlate structural features of Ni@Al₂O₃ composites (i.e., Ni-loading, particle size and shape; properties of Al₂O₃ supports and Ni/Al₂O₃ interface interactions; pre-catalysts calcination/reduction treatments and methods for Ni NPs deposition) with their methanation performance, the matter remains rather controversial. In a recent report, Beierlein and Traa have demonstrated how CO₂ conversion in methanation reactions promoted by highly Ni-loaded Al₂O₃-based composites is “insensitive” to the structure of the metal active phase.^[20] Their findings have contributed to reassess more traditional catalyst technologies based on less sophisticated synthetic strategies for the metal active phase **grown** at the surface of classical metal-oxide-based support.

In this contribution, we describe a RF-heated methanation scheme based on straightforwardly prepared Ni/ γ -Al₂O₃ composites featured by a relatively high nickel content (up to 40 wt%). The metal is present in the form of large and highly interconnected metal crystallites that cover part of γ -Al₂O₃ surface, acting as electrically conductive/magnetic susceptor for the electromagnetic energy conversion into heat (induction heating) while serving as robust, catalytically active sites for the methanation process to occur.

In addition, the poor thermal conductivity of γ -Al₂O₃ together with the fast heat control at the catalyst bed (ensured by the IH setup) allow for the harvesting of part of the surplus of energy (heat) generated by the reaction exothermicity. This extra-heat is then reused to keep the catalyst under isothermal conditions while reducing the reactor power supply. The rational heat management within the proposed methanation setup has ensured a highly efficient protocol for SNG production (X_{CO₂} up 98% with >99% S_{CH₄}) already under low operative temperatures (210–230 °C).

2. Results and Discussion

2.1. Highly Ni-loaded γ -Al₂O₃ composites: synthesis and characterization

Highly metal-loaded ^kNi/ γ -Al₂O₃ composites (k = 30 or 40 wt%) were straightforwardly prepared by wet impregnation followed by conventional thermal calcination/reduction steps (see Experimental Section, Materials and Methods for procedure details).

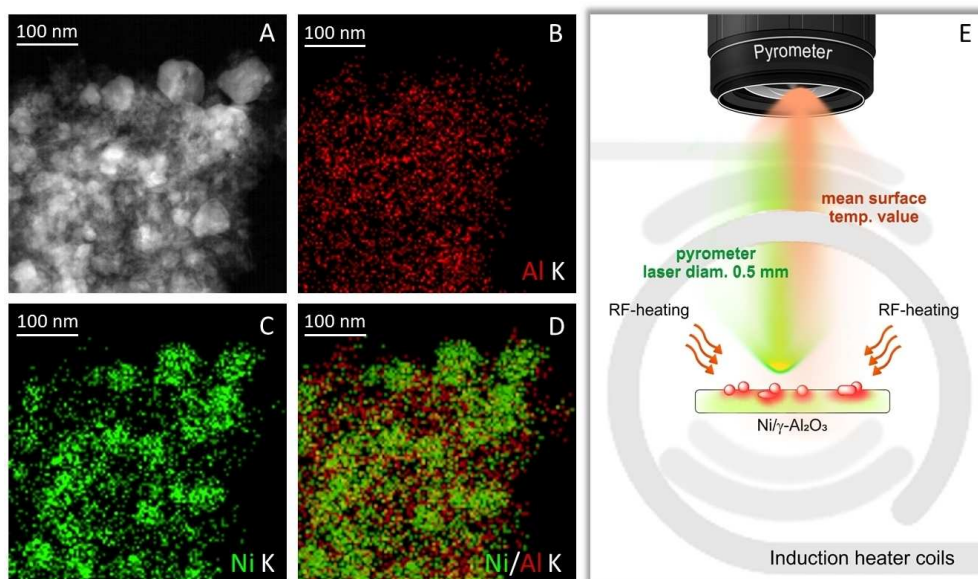


Figure 1. (A–D) Compositional elemental mapping of the most representative sample for catalysis application ($^{40}\text{Ni}/\gamma\text{-Al}_2\text{O}_3$, vide infra) A) Transmission electron microscopy (TEM) image of the composite where $\gamma\text{-Al}_2\text{O}_3$ domains can be observed. B–D) Scanning TEM energy-dispersive X-ray spectroscopy elemental mapping of Al–K, Ni–K and Ni/Al–K ionization edges. Ni–K indicates a homogeneously metal distribution in the sample along with the generation of large and highly interconnected aggregates. E) Temperature of the RF-heated Ni-susceptor on $\gamma\text{-Al}_2\text{O}_3$ as measured by a laser pyrometer (\varnothing laser beam: $\approx 500\ \mu\text{m}$, power $< 1\ \text{mW}$) located at $\approx 30\ \text{cm}$ from the catalyst. A standard calibration procedure^[23] has been used to fix the emissivity factor for each Ni-based catalyst used in the study.

Reduction of calcined samples was performed at $350\ ^\circ\text{C}$ under a pure stream of H_2 ($100\ \text{mL}\ \text{min}^{-1}$) for 3 h as to convert $^k\text{NiO}/\gamma\text{-Al}_2\text{O}_3$ pre-catalysts into their $^k\text{Ni}/\gamma\text{-Al}_2\text{O}_3$ counterparts. All composites were fully characterized by H_2 -TPR (Figure S1), XRD (Figure S2), TEM/STEM-EDS (Figures 1A–D and Figures S3A–D), N_2 -physisorption (Figure S4) and H_2 -chemisorption (Table 1). A full account on materials characterization is given, although discussion on more conventional details and analyses is moved to Supporting Information for the sake of shortness (see details in the captions of the respective figures/schemes).

Scanning transmission electron microscopy (STEM) combined with energy-dispersive X-ray spectroscopy (EDS) was used to monitor metal dispersion, showing pretty good and homogeneous distributions all over the scanned areas (Figure 1 and Figure S3). As expected, the higher the nickel loading the lower the catalyst metal dispersion and the larger the size of

nickel aggregates.^[19a,20, 21] The nickel surface area (S_{Ni} [$\text{m}^2\ \text{g}_{\text{Ni}}^{-1}$] and [$\text{m}^2\ \text{g}_{\text{cat}}^{-1}$]), metal dispersion (D [%]) and average Ni particles sizes (dP [nm]) were determined for each composite by H_2 chemisorption analysis (Table 1). Ni particle size steadily increases with the metal content^[22] while Ni exposed surface area and dispersion decrease accordingly.

2.2. RF-heated methanation operated at low temperatures

Highly Ni-loaded $\gamma\text{-Al}_2\text{O}_3$ catalysts were selected for operating methanation under low temperature conditions by joining the inherent magnetic/conductive and catalytic properties of the metal active phase with a RF-heating scheme. An induction heating setup equipped with a PID-interfaced (proportional integral derivative controller) laser pyrometer directly shot over

Table 1. BET surface areas, BJH total pore volumes and H_2 chemisorption data of $\gamma\text{-Al}_2\text{O}_3$ and its composites $^k\text{Ni}/\gamma\text{-Al}_2\text{O}_3$ at variable Ni loading ($k=30\text{--}40\ \text{wt}\ \%$).

Entry	Sample ^[a]	$S_{\text{Ni}}^{\text{[b]}}$ [$\text{m}^2\ \text{g}_{\text{Ni}}^{-1}$] ^[e]	$D^{\text{[b]}}$ [%]	$dP^{\text{[b]}}$ [nm]	SSA ^[c] [$\text{m}^2\ \text{g}^{-1}$]	$V_{\text{p}(\text{total})}^{\text{[d]}}$ [$\text{m}^3\ \text{g}^{-1}$]
1	$\gamma\text{-Al}_2\text{O}_3$	–	–	–	279	0.951
2	$^{30}\text{Ni}/\gamma\text{-Al}_2\text{O}_3$	42.6	12.4	6.4	183	0.491
3	$^{40}\text{Ni}/\gamma\text{-Al}_2\text{O}_3$	37.3	14.5	5.6	160	0.426
4 ^[f]	$^{40}\text{Ni}/\gamma\text{-Al}_2\text{O}_3$	35.3	14.1	5.1	n.d.	n.d.

[a] Except for the plain $\gamma\text{-Al}_2\text{O}_3$, all nickel composites underwent reduction at $350\ ^\circ\text{C}$ for 3 h in a constant stream of pure H_2 ($100\ \text{mL}\ \text{min}^{-1}$). [b] Measured by H_2 chemisorption analysis. [c] BET specific surface area (SSA) measured at $T=77\ \text{K}$. [d] Total pore volume determined by using the adsorption branch of N_2 isotherm at $p/p_0=0.98$. [e] These authors are aware that according to the International System of Units $\text{m}^2\ \text{g}_{\text{cat}}^{-1}$ is the correct unit for expressing the S_{Ni} value. However, we also referred to $\text{m}^2\ \text{g}_{\text{Ni}}^{-1}$ unit for the sake of comparison with other literature data. [f] $^{40}\text{Ni}/\gamma\text{-Al}_2\text{O}_3$ recovered after 60 h methanation reaction [catalysis conditions: IH at $210\ ^\circ\text{C}$; catalyst weight = 0.4 g, GHSV (STP) = $20000\ \text{mL}\ \text{g}_{\text{cat}}^{-1}\ \text{h}^{-1}$, $[\text{CO}_2]=20\ \%$, $[\text{H}_2]=80\ \%$, H_2 -to- CO_2 v/v ratio = 4].

the catalyst composites (Figure S5), was used to control the average catalyst temperature by finely tuning the applied IH power supply. This heating scheme allowed for an almost real-time control on the catalyst "hot spots" ignition throughout the exothermic catalytic runs, hence avoiding undesired temperature swings. In a typical methanation run, 0.4 g of $^k\text{Ni}/\gamma\text{-Al}_2\text{O}_3$ catalyst ($k=30\text{-}40$ wt%) were charged in a quartz tubular reactor housed inside the inductor coils and a H_2/CO_2 mixture (4 v/v ratio) was streamed downward through the catalyst bed at ambient pressure (1 atm) and at GHSVs comprised between 10000 and 30000 $\text{mL g}_{\text{cat}}^{-1} \text{h}^{-1}$.

Both composites showed good hyperthermic efficiency (i.e., their capacity to act as heat mediators^[8b,24] once immersed in an AC magnetic field), allowing rapid heating/cooling ramps (60–80 °C min^{-1}) in a relatively wide temperature range (150–230 °C for $^{30}\text{Ni}/\gamma\text{-Al}_2\text{O}_3$ and 150–270 °C for $^{40}\text{Ni}/\gamma\text{-Al}_2\text{O}_3$). Although the investigation on the nature of the electromagnetic dissipation phenomena at work in these highly metal-loaded composites is out of the scope of the present contribution, eddy currents (or Foucault currents)^[25] flowing through the electrical resistance of the large nickel aggregates (susceptor) are likely the main contribution responsible for the particles heating. However, given the nickel magnetic properties^[25,26] and its relatively high Curie temperature ($T_c =$

628 K),^[26] a contribution to particles heating from electromagnetic energy dissipation via hysteresis loss^[27] cannot be definitively ruled out.

CO_2 conversion (X_{CO_2}) and methane selectivity (S_{CH_4}) were initially measured in the 150–240 °C temperature range at ambient pressure, using a H_2/CO_2 ratio of 4 (v/v) at a GHSV = 20000 $\text{mL g}_{\text{cat}}^{-1} \text{h}^{-1}$. Catalysts performance (X_{CO_2} and S_{CH_4} of $^{30}\text{Ni}/\gamma\text{-Al}_2\text{O}_3$ and $^{40}\text{Ni}/\gamma\text{-Al}_2\text{O}_3$) along with the current (I [A]) supplied by the induction heater to keep the catalyst temperature constant at the target value are outlined in Figure 2A.

Under these conditions, both catalysts show increasing X_{CO_2} values while increasing the catalyst temperature and rapidly approach high conversions ($X_{\text{CO}_2} > 80\%$ for $^{40}\text{Ni}/\gamma\text{-Al}_2\text{O}_3$) with quantitative methane selectivity ($S_{\text{CH}_4} > 99\%$ for both Ni-samples) already under moderate operative temperatures (210 °C).

The catalyst temperature [as measured by the laser pyrometer (\emptyset laser beam: $\approx 500 \mu\text{m}$, power $< 1 \text{ mW}$)] is an average value given by the temperature of the metal-oxide (support) and that of the radiofrequency excited nickel particles on a relatively large section of the catalyst surface (Figure 1E). Although the real temperature of radio-frequency heated nano-objects remains a challenging matter to be addressed,^[8a,28] literature precedents for RF-heated transformations lead to

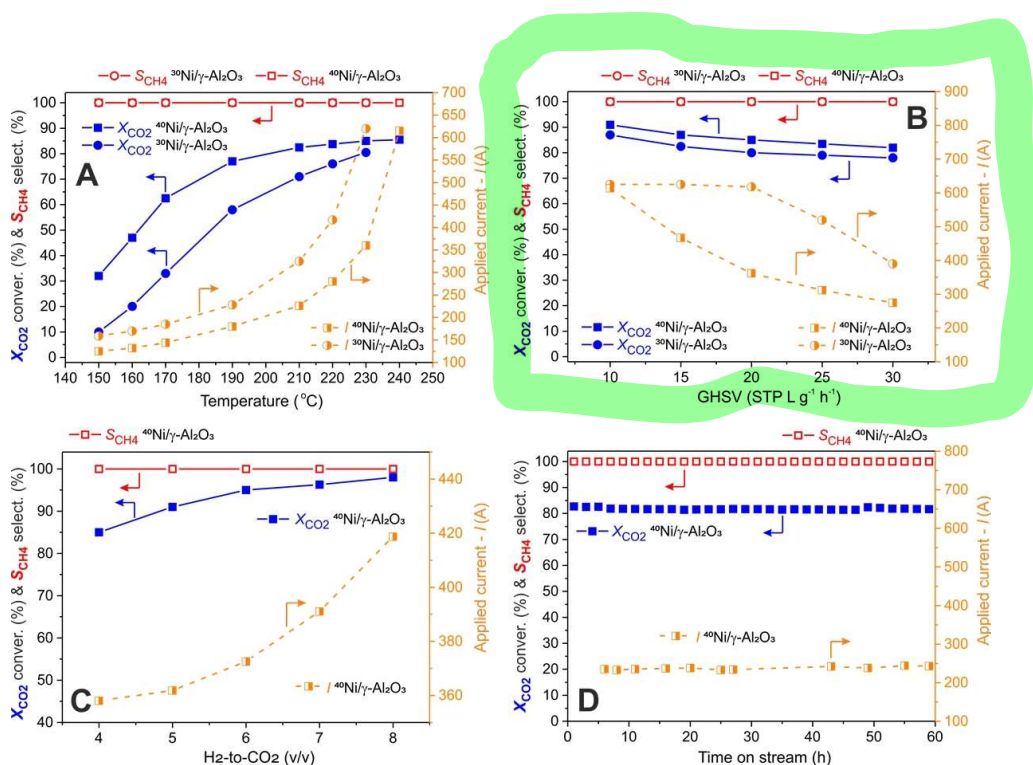


Figure 2. (A) CO_2 methanation runs with $^k\text{Ni}/\gamma\text{-Al}_2\text{O}_3$ ($k=30$ and 40 wt%) as catalysts operated under IH at variable reaction temperatures. Other reaction conditions: catalyst weight = 0.4 g, GHSV (STP) = 20000 $\text{mL g}_{\text{cat}}^{-1} \text{h}^{-1}$, $[\text{CO}_2] = 20\%$, $[\text{H}_2] = 80\%$, $\text{H}_2\text{-to-CO}_2$ v/v ratio = 4. (B) CO_2 methanation runs with $^k\text{Ni}/\gamma\text{-Al}_2\text{O}_3$ ($k=30$ and 40 wt%) as catalysts operated under IH, at variable GHSVs while keeping constant the catalyst temperature to 230 °C. Other reaction conditions: catalyst weight = 0.4 g (corresponding to 0.11 and 0.14 g of Ni for $^{30}\text{Ni}/\gamma\text{-Al}_2\text{O}_3$ and $^{40}\text{Ni}/\gamma\text{-Al}_2\text{O}_3$ samples, respectively), GHSVs (STP) = 10000–30000 $\text{mL g}_{\text{cat}}^{-1} \text{h}^{-1}$, $[\text{CO}_2] = 20\%$, $[\text{H}_2] = 80\%$, $\text{H}_2\text{-to-CO}_2$ v/v ratio = 4. (C) CO_2 methanation run with $^{40}\text{Ni}/\gamma\text{-Al}_2\text{O}_3$ as catalyst operated under IH at variable $\text{H}_2\text{-to-CO}_2$ v/v ratio from 4 to 8, reaction temperature: 230 °C. X_{CO_2} and S_{CH_4} given in Figures 2A–C refer to the catalyst steady-state-conditions after 4–6 h on run. (D) Long-term methanation reaction with $^{40}\text{Ni}/\gamma\text{-Al}_2\text{O}_3$ as catalyst operated under IH at 210 °C. Other reaction conditions: catalyst weight = 0.4 g, GHSV (STP) = 20000 $\text{mL g}_{\text{cat}}^{-1} \text{h}^{-1}$, $[\text{CO}_2] = 20\%$, $[\text{H}_2] = 80\%$, $\text{H}_2\text{-to-CO}_2$ v/v ratio = 4. Symbols: CO_2 conversion (X_{CO_2}): ■ for $^{40}\text{Ni}/\gamma\text{-Al}_2\text{O}_3$, ● for $^{30}\text{Ni}/\gamma\text{-Al}_2\text{O}_3$; CH_4 selectivity (S_{CH_4}): □ for $^{40}\text{Ni}/\gamma\text{-Al}_2\text{O}_3$, ○ for $^{30}\text{Ni}/\gamma\text{-Al}_2\text{O}_3$; Applied current (I [A]) at constant frequency (260 kHz), flowing the inductor coils and required to generate an electromagnetic field (B) necessary to heat $^{40}\text{Ni}/\gamma\text{-Al}_2\text{O}_3$ (■) or $^{30}\text{Ni}/\gamma\text{-Al}_2\text{O}_3$ (●), respectively, at the target (± 1 °C) temperature value.

suppose that the temperature of the nickel aggregates at the γ - Al_2O_3 surface (see Figure 1C) is reasonably higher than the average temperature value measured by the pyrometer.^[29]

Any temperature swing registered by the laser pyrometer at the catalyst bed (originated from the reaction exothermicity - particularly when methanation is operated under a discontinuous reagents supply) is suddenly and automatically compensated by the PID system through a fine tuning of the IH power supply. Such an accurate and rapid heat management directly at the catalytic sites brings important benefits to the process. It boosts the catalytic process to the bounds of its inherent kinetics^[8b] (while keeping the overall reactor temperature at lower values) and it allows part of the endogenous heat produced by the reaction to be harvested and conveyed for running the process itself instead of being totally wasted through dissipation (vide infra). In addition, the heat raised directly at the catalyst bed (from the nickel susceptor) implies the generation of a thermal gradient between the catalyst surface and the surrounding gaseous reagents and products. Such a thermal gradient, not present in classical joule-heated reactors, fosters a reduction of the steam partial pressure at the catalyst bed by favoring water condensation at the "cold-reactor"^[28b] and thus shifting the thermodynamic equilibrium towards the target product: methane [see Eq. (1) in Experimental Section]. This effect is likely at the origin of the highly efficient methanation scheme proposed.

The alternating current supplied to the IH setup and required to keep the temperature at the surface of the two composites at its target value (Figure 2A, orange dashed lines), highlights the different hyperthermic efficiency of the two samples at variable Ni-loading. The higher the Ni-loading the higher the catalyst hyperthermic response and hence the lower the current flowing through the inductor coil to reach and maintain the desired temperature at the catalytic bed.

Accordingly, the current supplied to the IH setup to heat $^{40}\text{Ni}/\gamma\text{-Al}_2\text{O}_3$ up to a given temperature value is systematically lower than that provided for its 30 wt% Ni-loaded counterpart ($^{30}\text{Ni}/\gamma\text{-Al}_2\text{O}_3$; Figure 2A). In addition, mean temperature values as high as 240 °C were reached and stably maintained on $^{40}\text{Ni}/\gamma\text{-Al}_2\text{O}_3$, whereas only temperatures up to a maximum of 230 °C can be stably reached with $^{30}\text{Ni}/\gamma\text{-Al}_2\text{O}_3$. The effect of reagents' GHSV on the methanation performance of RF-heated $^k\text{Ni}/\gamma\text{-Al}_2\text{O}_3$ ($k=30$ or 40 wt%) catalysts was determined at 230 °C under constant H_2 -to- CO_2 ratio of 4 v/v (Figure 2B). Results show how increased GHSVs (from 10000 to 30000 $\text{mL g}_{\text{cat}}^{-1} \text{h}^{-1}$) moderately decrease CO_2 conversions (from 91 to 82% for $^{40}\text{Ni}/\gamma\text{-Al}_2\text{O}_3$ and from 87 to 78% for $^{30}\text{Ni}/\gamma\text{-Al}_2\text{O}_3$), whereas S_{CH_4} is constantly 100%, whatever the gas rate and catalyst used. Notably, the current (orange dashed lines) supplied to the IH setup and required to maintain the catalyst at its operative temperature (230 ± 1 °C) decreases appreciably while GHSVs increase (from 614 to 275 A for $^{40}\text{Ni}/\gamma\text{-Al}_2\text{O}_3$ and from 625 to 390 A for $^{30}\text{Ni}/\gamma\text{-Al}_2\text{O}_3$). Such an I trends can be explained by assuming that the surplus of energy (heat) originated at the catalyst sites from the reaction exothermicity is not dissipated through the reactor walls but it is rather harvested (in part at least) and conveyed to run the process itself, maintaining the

catalyst temperature unchanged. Indeed, the higher the GHSV the higher the heat produced by the "controlled ignition" of local temperature gradients or "hot-spots" and then the lower the current supplied to the induction heater and needed to keep the catalyst under isothermal conditions. This is an example of a non-adiabatic system where the surplus of heat generated by the exothermicity of a catalytic process is deliberately gathered at the surface^[8b,30] of catalysts/susceptors and managed to run the process itself with an overall positive energy balance. This optimal heat (and energy) management is made possible by the IH setup that conjugates an almost real-time temperature monitoring at the catalyst bed (laser pyrometer) with the intensity of current (I [A]) supplied to its coils. In addition, the poor thermal conductivity of the $\gamma\text{-Al}_2\text{O}_3$ fosters the extra-heat harvesting at the catalytic sites by reducing energy waste phenomena owing to heat dissipation.

When methanation is operated at 230 ± 1 °C and constant GHSV ($20000 \text{ mL g}_{\text{cat}}^{-1} \text{h}^{-1}$), an increase of H_2 -to- CO_2 ratio (from 4 to 8 v/v) increases X_{CO_2} (from $X_{\text{CO}_2} = 85\%$ for H_2 -to- $\text{CO}_2 = 4$ to $X_{\text{CO}_2} = 98\%$ for H_2 -to- $\text{CO}_2 = 8$). However, the steadily reduced CO_2 concentration in the stream mirrors with a reduction of heat produced by the reaction exothermicity per unit mass of catalyst. Such a heat reduction is automatically compensated by an increase of the current flowing the inductor coils (from 358 to 419 A) to maintain the catalyst under isothermal conditions (Figure 2C). The increase of the current supplied is an indirect evidence of the role claimed above for the extra-heat generated by the reaction exothermicity (for methanation operated at increasing GHSVs; Figure 2B) and conveyed to run the methanation process. Overall, the proposed reaction scheme offers a more sustainable and radically different vision on how extra-heat produced by highly exothermic transformations can be handled. It allows to re-think the role of local temperature gradients (hot spots): from undesired phenomena responsible for energy waste to energy (heat) reservoirs for running the catalytic process more sustainably. Remarkably, the proposed scheme also provides a highly efficient and selective system for the methanation reaction with the possibility to operate the process already under relatively low temperatures.

Low-temperature operative conditions along with a fine control on temperature swings at the catalyst bed are important features that positively impact on the catalyst stability, its lifetime and hence on the process performance. Deactivation of heterogeneous catalysts is an ubiquitous problem that often causes loss of catalytic rate (particularly in the case of fixed-bed reactors operated under high-temperature conditions) and it generally requires costly and energy-consuming procedures for the catalyst regeneration if not for its complete substitution.^[31]

In particular, Ni-based catalysts for CO_2 methanation suffer from high-temperature induced deactivation phenomena such as "coking" and metal-particle sintering that may decline their performance over time.^[18a,32] In a model catalytic run (Figure 2D), $^{40}\text{Ni}/\gamma\text{-Al}_2\text{O}_3$ was used at 210 °C (average recorded temperature) at $20000 \text{ mL g}^{-1} \text{h}^{-1}$ as GHSV ($\text{H}_2/\text{CO}_2 = 4$) while keeping constant its initial performance ($X_{\text{CO}_2} = 83\%$; $S_{\text{CH}_4} = 100\%$) without any appreciable deactivation even after 60 h on

stream. Such a catalyst stability accounts for negligible deactivation phenomena related to undesired catalyst fouling (coking) or metal particle sintering. Fouling owing to the formation of carbon deposits was determined on the used $^{40}\text{Ni}/\gamma\text{-Al}_2\text{O}_3$ catalysts by thermogravimetric analysis (TGA) in air (100 mL min^{-1}) while H_2 -chemisorption was used to address any catalyst active phase alteration in terms of S_{Ni} , D and dP (Table 1, entry 3 vs. 4).

TG curves of the reduced catalyst before and after 60 h on methanation run are outlined in Figure S6. The TG analysis of the simply calcined $^{40}\text{Ni}/\gamma\text{-Al}_2\text{O}_3$ catalyst is also reported at comparison for the sake of completeness. Both fresh and used $^{40}\text{Ni}/\gamma\text{-Al}_2\text{O}_3$ present largely superimposable profiles with only minor deviations in the $150\text{--}350\text{ }^\circ\text{C}$ temperature range. This result confirms only negligible weight loss differences in the used sample respect to its pristine counterpart. H_2 -chemisorption on the used $^{40}\text{Ni}/\gamma\text{-Al}_2\text{O}_3$ finally accounts for moderately decreased S_{Ni} and D , whereas dP slightly increases with respect to the pristine sample (Table 1, entry 4 vs. 3). Moderate increase (3.9%) of crystallite sizes in the used catalyst can be attributed to the migration of smallest particles featuring with reduced support interactions (see H_2 -TPR in Figure S1) and their subsequent coalescence during the first hours on stream^[31] with only minor alterations (decrease) of the exposed nickel surface area. This control on the catalyst morphology and stability is also ensured by the presence of large particles aggregates in the highly Ni-loaded composites that reduced metal particles surface mobility. Accordingly, alterations of the catalyst active phase are deeply mitigated, its performance is preserved over long term runs and environmental risks associated to nano-objects leaching phenomena are markedly reduced.^[33]

For the sake of completeness and with the aim at validating the achievements coming from the implementation of the proposed catalyst technology in combination with an IH setup, the $^{40}\text{Ni}/\gamma\text{-Al}_2\text{O}_3$ catalyst was tested under identical reaction conditions using a more traditional heating setup: an oven (Joule heating, JH). To this aim, 0.4 g of $^{40}\text{Ni}/\gamma\text{-Al}_2\text{O}_3$ were charged in a quartz tubular reactor and the system was housed inside the electrical oven. For these trials, the temperature of the system was monitored by two independent thermocouples, one in the oven (T_1) and a further one located inside the catalytic bed (T_2) for the oven temperature regulation. Before operating each catalytic run, the catalyst was allowed to reach the target temperature and stabilize under a pure stream of He (see Experimental Section for details). As Figure 3 shows, when catalysis was operated at low-medium temperature values ($150\text{--}220\text{ }^\circ\text{C}$) X_{CO_2} measured with the Joule-heated system was markedly lower compared to conversions given under IH. Most importantly, the conversion values we appreciated under JH modality (always negligible below $200\text{ }^\circ\text{C}$) were more than 15 times lower than those measured under a IH regime (i.e., $X_{\text{CO}_2} = 5\%$ under JH vs. 77% under IH at the formal temperature of $210\text{ }^\circ\text{C} \pm 3\text{ }^\circ\text{C}$). Under low operative temperatures, the oven (T_1) and the catalyst (T_2) temperatures remained almost identical when the catalyst came in contact with the reactants mixture. On the other hand, when the oven (and catalyst) temperature increased to $230\text{ }^\circ\text{C}$ and the catalyst met the reagents mixture,

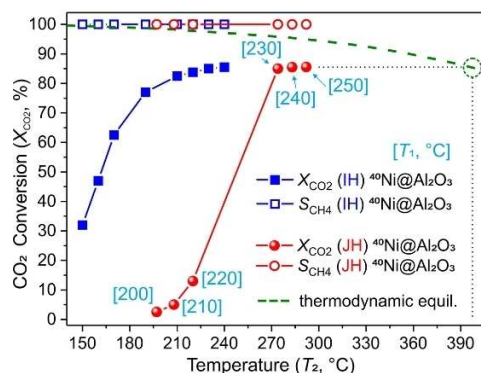


Figure 3. CO_2 methanation runs with $^{40}\text{Ni}/\gamma\text{-Al}_2\text{O}_3$ as catalysts operated at variable reaction temperatures under either IH or JH with an external oven. Other reaction conditions common to both reactor schemes: catalyst weight = 0.4 g, GHSV (STP) = $20000\text{ mL g}_{\text{cat}}^{-1}\text{ h}^{-1}$, $[\text{CO}_2] = 20\%$, $[\text{H}_2] = 80\%$, H_2 -to- CO_2 v/v ratio = 4, ambient pressure. Green dashed line refers to the thermodynamic equilibrium for a methanation process operated at ambient pressure and H_2 -to- CO_2 v/v ratio = 4.^[34] Values in light-blue square brackets are the setting temperatures measured by thermocouple T_1 ($\pm 1\text{ }^\circ\text{C}$) located inside the oven.

the average temperature measured at the catalytic bed (T_2) increased suddenly over $270\text{ }^\circ\text{C}$ and X_{CO_2} grew up to 86%. A further increase of the oven temperature (up to $250\text{ }^\circ\text{C}$) just led to an increase of the temperature catalytic bed, without any appreciable change in X_{CO_2} . Such a result suggests that nickel sites temperature goes beyond the mean value measured by the internal regulation thermocouple (T_2). Given the technical limits in measuring the effective temperature of nano-objects (whatever the heating setup used), it can be inferred that that of nickel sites ranges between the mean value measured by the thermocouple (T_2 ; $270\text{ }^\circ\text{C}$) and that at the thermodynamic equilibrium of a process operated at ambient pressure with a H_2/CO_2 of 4 for which a maximum $X_{\text{CO}_2} \approx 86\%$ is provided ($\approx 400\text{ }^\circ\text{C}$).^[34] A similar conclusion applies to the temperature of nickel sites under IH setup. However, the “contactless” induction heater besides ensuring a more rapid heat on/off switch directly at the catalytic sites, reduces markedly the thermal inertia required to re-establish the setting temperature compared to any traditional conduction/convection/radiation heating scheme (oven, JH).

The higher temperature control at the catalytic sites ensured by IH is finally witnessed by a progressive X_{CO_2} increase while increasing the catalyst temperature in the scrutinized temperature range ($150\text{--}230\text{ }^\circ\text{C}$). The reactivity gap between the two reactors at comparison deserves to be considered in light of the “cold catalysis” concept too.^[28b] Cold catalysis (that applies to IH) implies that energy is supplied directly to a responding susceptor (catalytic sites) suitable at the same time to catalyze the process while the external reactor walls are kept cold (“cold reactor”) and the thermal decomposition of gaseous reagents is significantly reduced.^[8b,35] As discussed above, this feature holds important effects from the viewpoint of the underlying catalytic mechanism at work, the catalyst performance and its lifetime on stream.

Although these authors are aware that any comparison with related heterogeneous systems from the state-of-the-art is hard to be exhaustively addressed owing to different conditions used (catalyst synthesis, operational conditions and reactor setup), a careful analysis of literature results unveils the unique performance (X_{CO_2} and S_{CH_4}) of our catalytic/reactor scheme. There are no doubts that radiofrequency heated catalysts are largely limited by the process kinetics rather than by heat transfer phenomena as typically occurs with more traditionally-heated (Joule-heated) reactors.^[8b] CO_2 methanation performance with $^{40}\text{Ni}/\gamma\text{-Al}_2\text{O}_3$ as catalyst (X_{CO_2} , S_{CH_4} and catalyst productivity expressed as $\text{mol}_{\text{CH}_4}\cdot\text{g}_{\text{Ni}}^{-1}\cdot\text{h}^{-1}$) is summarized in Table 2 and compared with the most representative Ni-based/ $\gamma\text{-Al}_2\text{O}_3$ catalysts reported so far as methanation systems to be operated under low-medium temperature conditions (typically in the 200–275 °C temperature range).

From these data it can be argued that the RF-heated $^{40}\text{Ni}/\gamma\text{-Al}_2\text{O}_3$ largely outperforms all benchmark systems based on classical Ni@ $\gamma\text{-Al}_2\text{O}_3$ catalysts operated under conventional heating schemes (Table 2, entries 1–10 vs. 17, 32–33, 43–44, 51–52 and 57–58), including all various Zr/Ce-promoted counterparts as well as engineered systems prepared from costly, sophisticated and less sustainable synthetic procedures (Table 2). Noteworthy, the proposed methanation scheme gives from pretty good to excellent performance already for temperature values (150–230 °C) largely below those commonly required to run the reaction efficiently. Given the relatively high flow-rates admitted in our reactor scheme (from 133 to 200 $\text{mL}\cdot\text{min}^{-1}$), X_{CO_2} , S_{CH_4} and productivity (λ) are markedly higher (for similar or identical H_2 -to- CO_2 ratio) than those claimed for methanation systems of the state-of-the-art and expressly conceived to operate the process under low temperature values (Table 2, entries 5 and 9 vs. 14–16, 36–37, 45, 49–50 and 68–69). For the sake of completeness, Figure 4 provides a snapshot of the performance recorded with our methanation protocol at comparison with literature outcomes (at least for processes carried out under low-medium temperature condi-

tions and for those references where productivities are provided or catalytic details are given for the relative λ calculation).

3. Conclusions

Re-thinking a chemical process in light of straightforwardly prepared and robust catalytic materials based on abundant and cheap components while minimizing energy waste and ensuring high catalytic performance under mild operative conditions are key objectives in heterogeneous catalysis. This contribution combines straightforwardly prepared catalysts based on non-critical raw materials with a less conventional heating scheme (IH - induction heating). A conceptually new and energy-efficient handling of the extra-heat produced by a highly exothermic process directly at the catalytic bed has allowed to setup of an efficient CO_2 methanation protocol for SNG production (X_{CO_2} up 98% with $>99\%$ S_{CH_4}) already at operative temperatures (150–230 °C) much lower than those commonly claimed for related systems in the literature. The heat targeting directly at the nickel susceptor is likely at the origin of the outstanding performance of the proposed methanation scheme. Indeed, the generation of a thermal gradient between the hot catalyst surface and its colder gaseous surrounding is supposed to reduce the partial pressure of steam at the catalyst bed, favoring water condensation at the outlet of the “cold-reactor” and shifting the thermodynamic equilibrium towards methane.

In addition, this powerful heating tool allows to overcome heat transfer limitations encountered in classical heating schemes (i.e., flame and resistance heating or traditional furnaces) and deeply reduces those secondary reaction paths (i.e., “cracking/decomposition/polymerization”) that seriously compromise the catalyst stability and life-cycle (“catalyst coking”).

The highly Ni-loaded $\gamma\text{-Al}_2\text{O}_3$ composites prepared by wet impregnation and featured by moderate metal dispersions and large metal aggregates play a dual role in the methanation scheme: they act as electrically conductive/magnetic susceptor for the electromagnetic energy conversion into heat (induction heating) and serve as robust “structure insensitive” active sites for the catalytic process to occur. The poor thermal conductivity of $\gamma\text{-Al}_2\text{O}_3$ support and the fast heat control at the catalyst bed ensured by the IH setup, finally allow for the recycling of part of the surplus of energy (heat) generated by the reaction exothermicity to keep the catalyst under virtual isothermal conditions.

Accordingly, the reactor power supply can be reduced and energy waste owing to heat dissipation paths is limited. These unique features linked to IH technology and its rational implementation to flow-reactor setup boost the catalytic processes to the bounds of their kinetics while keeping a low reactor walls temperature.

Such a scheme for the heat management in flow-reactors allows to re-evaluate industrially attractive composites (and their large-scale preparation methods) for catalytic application to key processes at the heart of P2G chain. Moreover, the virtual

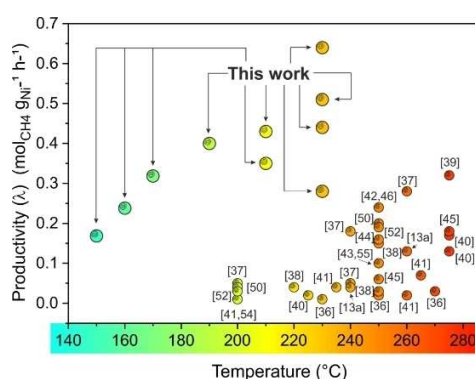


Figure 4. CO_2 methanation performance of the radiofrequency heated $^{40}\text{Ni}/\gamma\text{-Al}_2\text{O}_3$ composite at comparison with traditionally heated (promoted or unpromoted) Ni-based/ $\gamma\text{-Al}_2\text{O}_3$ catalysts of the state-of-the-art operating in the 150–275 °C temperature range. For numbers in the figure, refer to references quoted on Table 2.

Table 2. Catalyst performance (X_{CO_2} and S_{CH_4}) and productivity values expressed in terms of $\text{mol}_{\text{CH}_4} \text{g}_{\text{Ni}}^{-1} \text{h}^{-1}$ for Ni/Al₂O₃ composites from the literature prepared under variable conditions, using variable metal loadings and catalysts' promoters and selected among the systems for operating methanation under unconventional low-temperature conditions (typically in the 200–275 °C temperature range).

Entry	(Ni [wt %]) ^(a) Catalyst name ^(b) [charged cat. [mg]] ^(c)	T [°C]	Flow rate [mL min ⁻¹]	CO ₂ /H ₂ / inert [mL min ⁻¹]	H ₂ / CO ₂ v/v	GHSV [mL g ⁻¹ h ⁻¹]	X _{CO₂} [h ⁻¹]	S _{CH₄} [%]	λ	STY ^(d) [mol CH ₄ L ⁻¹ h ⁻¹]	Ref.	
1	(34.4) ⁴⁰ Ni/γ-Al ₂ O ₃ [400]	150	133.35	26.7/106.7/0	4	20000	17 700	32	100	(0.17) ^(e)	50.6	
2	(34.4) ⁴⁰ Ni/γ-Al ₂ O ₃ [400]	160	133.35	26.7/106.7/0	4	20000	17 700	47	100	(0.24) ^(e)	74.2	
3	(34.4) ⁴⁰ Ni/γ-Al ₂ O ₃ [400]	170	133.35	26.7/106.7/0	4	20000	17 700	62.5	100	(0.32) ^(e)	98.7	
4	(34.4) ⁴⁰ Ni/γ-Al ₂ O ₃ [400]	190	133.35	26.7/106.7/0	4	20000	17 700	77	100	(0.40) ^(e)	121.6	
5	(34.4) ⁴⁰ Ni/γ-Al ₂ O ₃ [400]	210	133.35	26.7/106.7/0	4	20000	17 700	82.5	100	(0.43) ^(e)	130.3	
6	(34.4) ⁴⁰ Ni/γ-Al ₂ O ₃ [400]	210	133.35	19.1/114.3/0	6	20000	17 700	95	100	(0.35) ^(e)	107.4	this work
7	(34.4) ⁴⁰ Ni/γ-Al ₂ O ₃ [400]	230	133.35	26.7/106.7/0	4	20000	17 700	85	100	(0.44) ^(e)	134.3	
8	(34.4) ⁴⁰ Ni/γ-Al ₂ O ₃ [400]	230	133.35	14.8/103.7/0	8	20000	17 700	98	100	(0.28) ^(e)	85.8	
9	(34.4) ⁴⁰ Ni/γ-Al ₂ O ₃ [400]	230	200	40/160/0	4	30000	26 550	82	100	(0.64) ^(e)	194.1	
10	(34.4) ⁴⁰ Ni/γ-Al ₂ O ₃ [400]	230	200	28.6/171.4/0	6	30000	26 550	91	100	(0.51) ^(e)	154.0	
11		230	100	1/50/49	50	60000	–	4	98	(0.01)		
12	(10) Ni/γ-Al ₂ O ₃ [100]	250	100	1/50/49	50	60000	–	7	98	(0.02)		[36]
13		270	100	1/50/49	50	60000	–	13	98	(0.03)		
14	(7.9) Ni/Al ₂ O ₃ -ZrO ₂ -1.0	200	50	10/40/0	4	6000	–	8	100	(0.05)		
15	[500]	240	50	10/40/0	4	6000	–	26	100	(0.18)		[37]
16		260	50	10/40/0	4	6000	–	42	100	(0.28)		
17 ^(f)	(7.3) Ni/γ-Al ₂ O ₃ [500]	240	50	10/40/0	4	6000	–	7	100	(0.05)		
18	(13.6) Ni14LA [88.2]	220	80	4.8/19.2/56	4	54420	–	4	100	(0.04)		
19		250	80	4.8/19.2/56	4	54420	–	14	100	(0.15)		[38]
20 ^(g)	(20) Ni/γ-Al ₂ O ₃ [88.2]	250	80	4.8/19.2/56	4	54420	–	4.2	100	(0.03)		
21	(15) Ni/Al ₂ O ₃ -S [100]	250	100	20/80/0	4	60000	–	< 1	100	–		
22		275	100	20/80/0	4	60000	–	9	100	(0.32)		
23	(15) Ni/Al ₂ O ₃ -P [100]	250	100	20/80/0	4	60000	–	< 1	100	–		[39]
24		275	100	20/80/0	4	60000	–	< 1	100	–		
25	(10.9) Ni/Al ₂ O ₃ [500]	225	300	40/200/60	5	36000	–	< 1	98	–		
26		275	300	40/200/60	5	36000	–	7	98	(0.13)		
27	(18.5) Ni/Al ₂ O ₃ [500]	225	300	40/200/60	5	36000	–	2	98	(0.02)		[40]
28		275	300	40/200/60	5	36000	–	15	98	(0.17)		
29		200	40	6/24/10	4	2400	–	16	99.5	(0.01)		
30	(20) Ni/H – Al ₂ O ₃ [1000]	235	40	6/24/10	4	2400	–	50	99.5	(0.04)		
31		265	40	6/24/10	4	2400	–	90	99.5	(0.07)		[41]
32 ^(h)	(20) Ni/γ-Al ₂ O ₃ [1000]	200	40	6/24/10	4	2400	–	10	99.5	(0.01)		
33 ⁽ⁱ⁾		260	40	6/24/10	4	2400	–	20	99.5	(0.02)		
34	(16.6) Ni/Al ₂ O ₃ [300]	200	300	30/120/150	4	60000	–	< 1	100	–		[42]
35		250	300	30/120/150	4	60000	–	15	97.5	(0.24)		
36	(10) MA-10Ni [100]	200	25	5/20/0	4	15000	–	< 1	94.8	–		[43]
37		250	25	5/20/0	4	15000	–	8	94.5	(0.10)		
38	(78) Ni-Al ₂ O ₃ -HT [40]	200	50	9/36/5	4	75000	–	5	–	–		[44]
39		250	50	9/36/5	4	75000	–	21	98.6	(0.16)		
40		220	50	10/40/0	4	30000	–	< 1	99	–		
41	(12) NiCe/Al ₂ O ₃ [100]	240	50	10/40/0	4	30000	–	2	93	(0.04)		
42		260	50	10/40/0	4	30000	–	6	95	(0.13)		[13a]
43 ^(j)	(12) Ni/γ-Al ₂ O [100]	240	50	10/40/0	4	30000	–	< 1	–	n.d.		
44 ^(k)		260	50	10/40/0	4	30000	–	2	–	n.d.		
45	(12) Ni/Al ₂ O ₃ [150]	250	140	20/80/40	4	56000	–	2	100	(0.06)		[45]
46		275	140	20/80/40	4	56000	–	6	100	(0.18)		
47	(10) Ni/Al ₂ O ₃ [150]	200	600	30/120/450	4	240000	–	< 1	100	–		[46]
48		250	600	30/120/450	4	240000	–	5	90	(0.24)		
49	(–) Ni ₅ -AIMO [500]	200	40	6/24/10	4	4800	–	30	100	n.d.		
50		250	40	6/24/10	4	4800	–	89.4	99	n.d.		[47]
51 ^(l)	(–) Ni/γ-Al ₂ O ₃ [500]	200	40	6/24/10	4	4800	–	4	99	n.d.		
52 ^(m)		250	40	6/24/10	4	4800	–	8	99	n.d.		
53	(13.8) Ni16 [44]	250	n.d.	n.d.	5	–	52 300	1	100	n.d.		[48]
54		200	n.d.	n.d.	3.5	8100	–	< 1	> 99	n.d.		
55	(12) Ni/ZA-3 [n.d.]	240	n.d.	n.d.	3.5	8100	–	8	> 99	n.d.		[49]
56		275	n.d.	n.d.	3.5	8100	–	25	> 99	n.d.		
57 ⁽ⁿ⁾	(12) Ni/γ-Al ₂ O ₃ [n.d.]	200	n.d.	n.d.	3.5	8100	–	–	> 99	n.d.		

Table 2. continued

Entry	(Ni [wt %]) ^[a] Catalyst name ^[b] [charged cat. [mg]] ^[c]	T [°C]	Flow rate [mL min ⁻¹]	CO ₂ /H ₂ / inert [mL min ⁻¹]	H ₂ / CO ₂ v/v	GHSV [mL g ⁻¹ h ⁻¹]	X _{CO₂} [h ⁻¹]	S _{CH₄} [%]	λ [mol CH ₄ g _{Ni} ⁻¹ h ⁻¹]	STY ^[d] [mol CH ₄ L ⁻¹ h ⁻¹]	Ref.
58 ^[o]		240	n.d.	n.d.	3.5	8100	–	< 1	> 99	n.d.	
59	(15) Ni-2CeO ₂ /Al ₂ O ₃ [200]	200	50	10/40/0	4	15000	–	5	100	(0.04)	[50]
60		250	50	10/40/0	4	15000	–	22	100	(0.20)	
61	(20) Ni/Al ₂ O ₃ [n.d.]	200	n.d.	n.d.	3.5	9000	–	8	100	n.d.	[51]
62		250	n.d.	n.d.	3.5	9000	–	41	100	n.d.	
63	(20) Ni/Al ₂ O ₃ [200]	200	30	6.7/23.3/0	3.5	9000	–	7.1	100	(0.03)	[52]
64		250	30	6.7/23.3/0	3.5	9000	–	42	100	(0.19)	
65	(12) Ni/Al ₂ O ₃ [n.d.]	250	100	5/20/75	4	–	–	33	98	n.d.	[53]
66		200	30	6.7/23.3/0	3.5	9000	–	2	100	(0.01)	
67	(25) Ni/Al ₂ O ₃ [200]	250	30	6.7/23.3/0	3.5	9000	–	8	100	(0.03)	[54]
68		200	25	5/20/0	4	15000	–	< 1	95	n.d.	[55]
69	(10) OMA-10Ni [100]	250	25	5/20/0	4	15000	–	8	95	(0.10)	
70		250	200	20/80/100	4	13043	9554	38	100	(0.11)	
71	(20) Ni/Al ₂ O ₃ [920]	275	200	20/80/100	4	13043	9554	83	100	(0.24)	[56]

[a] wt% of Ni particles in the catalyst. [b] Catalyst acronym. [c] mg of catalyst used in CO₂ methanation. [d] Values in curly brackets refer to the reactor performance expressed as space-time yield (STY n_{CH_4} [mol]/(V_{cat} [L]·t [h])^[e]). The volume of 0.4 g of ⁴⁰Ni/γ-Al₂O₃ is equal to 0.452 mL (see experimental section for details). [e] Productivity values are calculated according to the exact catalyst metal loading determined by ICP-OES analysis on ⁴⁰Ni/γ-Al₂O₃ (34.4 wt%). [f] Comparative analysis between Ni/Al₂O₃ catalyst synthesized by a single-step epoxide-driven sol-gel method and its ZrO₂-promoted counterpart (see entry 15). [g] Comparative analysis between Ni/Al₂O₃ catalyst synthesized by incipient impregnation method and its La-promoted counterpart (see entry 19). [h] Comparative analysis between Ni/Al₂O₃ catalyst synthesized by classical impregnation method and supported Ni nanoparticles on a hierarchical flowerlike Al₂O₃ matrix (see entry 29). [i] Comparative analysis between Ni/Al₂O₃ catalyst synthesized by classical impregnation method and supported Ni nanoparticles on a hierarchical flowerlike Al₂O₃ matrix (see entry 31). [j] Comparative analysis between Ni/Al₂O₃ catalyst synthesized by classical impregnation method and its Ce-promoted counterpart (see entry 41). [k] Comparative analysis between Ni/Al₂O₃ catalyst synthesized by classical impregnation method and its Ce-promoted counterpart (see entry 42). [l] Comparative analysis between Ni/Al₂O₃ catalyst synthesized by classical impregnation method and its Ni₂-AIMO counterpart prepared by hydrothermal synthesis method (see entry 49). [m] Comparative analysis between Ni/Al₂O₃ catalyst synthesized by classical impregnation method and its Ni₂-AIMO counterpart prepared by hydrothermal synthesis method (see entry 50). [n] Comparative analysis between Ni/Al₂O₃ catalyst synthesized by classical impregnation method and its ZrO₂-promoted counterpart (see entry 54). [o] Comparative analysis between Ni/Al₂O₃ catalyst synthesized by classical impregnation method and its ZrO₂-promoted counterpart (see entry 55). n.d.: “not determined” or “not determinable” on the basis of the data available on the original papers.

absence of any reactants pre-heating (until they come in close contact with the catalyst/susceptor) makes this operational mode highly attractive for other challenging catalytic processes (e. g. methane dehydro-aromatization or methane reforming).

Experimental Section

Materials and methods

Synthesis of ^kNi/γ-Al₂O₃ composites. In a typical procedure, 1 g of γ-Al₂O₃ (Ketjen CK-300B, Akzo Nobel, S_{BET} = 279 ± 10 m² g⁻¹) in the form of extruded trilobes (≈ 1 mm × ≈ 4 mm) was finely crushed and sieved to get a tiny powder (≈ 80–140 μm) to be impregnated with Ni(NO₃)₂·6H₂O aqueous solutions at variable salt concentration (0.011 and 0.007 mol of Ni salt precursor for ⁴⁰Ni/γ-Al₂O₃ and ³⁰Ni/γ-Al₂O₃, respectively). For each sample, the volume of Ni saltwater solution was significantly higher than the total pore volume of γ-Al₂O₃ support. Suspensions were evaporated and samples oven-dried at 120 °C for 12 h before being calcined in air at 350 °C for 2 h (heating rate for drying and calcination: 3 °C min⁻¹) as to convert the nickel salt into the corresponding oxide. The as obtained ^kNiO/γ-Al₂O₃ pre-catalysts (k = 30 or 40 Ni wt%) were converted into the ^kNi/γ-Al₂O₃ counterparts under a pure H₂ flow (100 mL min⁻¹) at 350 °C for 3 h immediately before each CO₂ methanation test.

Characterization methods. Hydrogen temperature programmed reduction (H₂-TPR) was performed on a chemisorption analyzer (Micromeritics AutoChem II) coupled with a thermal conductivity

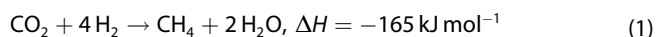
detector (TCD). In a typical experiment, 50 mg of sample were loaded in a quartz tube and heated at 100 °C for 30 min. Afterwards, a 10% (v/v) H₂/Ar gas mixture was flowed (30 mL min⁻¹) through the sample and the temperature increased to 800 °C (heating rate: 5 °C·min⁻¹) and H₂ consumption was registered throughout the reduction process. Powder X-ray Diffraction (PXRD) measurements were carried out on a Bruker D-8 Advance diffractometer equipped with a Vantec detector (Cu Kα radiation) working at 40 kV and 40 mA. X-ray diffractograms were recorded in the 2θ–80° 2θ region at room temperature in air. Transmission Electron Microscopy (TEM) was carried out on a Titan Themis ETEM G3 (ThermoFisher) microscope working at 300 kV accelerated energy dispersive X-ray spectroscopy (EDS) was conducted on Ultim Max TEM Silicon Drift Detector (SDD) (Oxford, 80 mm²) equipped on the microscope. Elemental signals were extracted from the Al–K, Ni–K and Ni/Al–K ionization edges. For these measurements, samples were dispersed in ethanol, sonicated for a few minutes before drop-casting the obtained homogeneous suspensions on a copper grid covered with a holey carbon membrane. The BET SSA were calculated from N₂ physisorption isotherms recorded at 77 K on an ASAP 2020 Micromeritics instrument. Pore size distribution was determined by Barrett-Joyner-Halenda (BJH) method. All samples were degassed/activated at 250 °C for 6 h prior each measurement. Nickel surface area (S_{Ni} [m² g_{Ni}⁻¹]), metal dispersion (D [%]) and average Ni particle size (dP [nm]) were determined by H₂ chemisorption analyses conducted on an ASAP 2020 Micromeritics instrument. Samples were pre-treated in a H₂ flow for 3 h at 350 °C and the adsorption isotherms were recorded at 35 °C. The Ni surface area was determined from the total amount of adsorbed H₂ extrapolated to zero pressure after subtracting the contribution of physisorbed H₂ and assuming a Ni/H = 1 stoichiometry and a 6.49 Å² nickel cross-

sectional area. Inductively coupled plasma optical emission spectrophotometry (ICP-OES) measurements on mineralized $^k\text{NiO}/\gamma\text{-Al}_2\text{O}_3$ pre-catalysts were accomplished on a Varian 720 ES ICP-OES instrument. The effective nickel charges for $^{30}\text{Ni}/\gamma\text{-Al}_2\text{O}_3$ and $^{40}\text{Ni}/\gamma\text{-Al}_2\text{O}_3$ were then fixed to 27.5 and 34.4 wt%, respectively. TGA was run under air (100 mL min^{-1}) on an EXSTAR thermogravimetric analyzer (TG/DTA) Seiko 6200.

Induction heating setup. The induction heating setup (EasyHeat 8310, 10 kW, Ambrell Ltd) is constituted by a spiral 6-turn induction coil (length = 1.05 m, pure coil resistance = $2.066 \times 10^{-3}\ \Omega$), cooled by means of an external chiller with recirculated water/glycerol (10%) mixture. In a typical experiment, the quartz reactor containing the catalyst was housed inside the induction heater coils and temperature real-time control/regulation was ensured by a PID system (Proportional Integral Derivative controller, Eurotherm model 3504) connected to a laser pyrometer (Optris, \varnothing laser beam: $\approx 500\ \mu\text{m}$, power < 1 mW, located at $\approx 30\text{ cm}$ from the catalyst) shot up on the catalyst bed and working in the $150\text{--}1000\text{ }^\circ\text{C}$ range (accuracy $\pm 1\text{ }^\circ\text{C}$). The heating/cooling rate allowed for the system is $60\text{--}80\text{ }^\circ\text{C min}^{-1}$ in the $150\text{--}300\text{ }^\circ\text{C}$ temperature range.

Joule heating setup (electrical oven). Methanation trials under classical heating setup were carried out using an external electrical oven (ERALY Co., $\varnothing_{\text{OD}} = 200\text{ mm}$; $\varnothing_{\text{ID}} = 55\text{ mm}$; depth: 300 mm; $I_{\text{max}} = 8.6\text{ A}$, $T_{\text{max}} = 1100\text{ }^\circ\text{C}$). $^{40}\text{Ni}/\gamma\text{-Al}_2\text{O}_3$ charged in a quartz tubular reactor was housed inside the oven. The temperature of the system was monitored by two type-K thermocouples, one for regulating the oven temperature (T_1) and an additional one located inside the catalytic bed (T_2) for measuring the temperature swings throughout the process. For these trials, we used thermocouples of $\varnothing_{\text{ED}} = 0.5\text{ mm}$, very close to the dimension of the laser pyrometer spot in IH. Before each catalytic run, catalyst was allowed to reach and stabilize (30–45 min) at the target temperature under a pure stream of He (max temperature deviation recorded between T_1 and T_2 after stabilization = $\pm 3\text{ }^\circ\text{C}$).

Catalytic tests. CO_2 methanation reaction [Eq. (1)] was conducted at atmospheric pressure in a fixed-bed quartz tubular reactor [$\varnothing_{\text{ID}} = 12\text{ mm}$, length = 400 mm] charged with 0.4 g of $^k\text{Ni}/\gamma\text{-Al}_2\text{O}_3$ catalyst ($k = 30\text{--}40\text{ wt\%}$),^[57] equipped with an advanced EasyHeat 8310 induction heating setup or a classical external furnace.



Whatever the heating system used, prior of each methanation test, the pre-catalyst was reduced under a stream of pure hydrogen (100 mL min^{-1}) for 3 h at $350\text{ }^\circ\text{C}$. Heat for the reduction step was provided by an external electric furnace. In a typical procedure, a H_2/CO_2 gas mixture (from 4 to 8 v/v) at variable GHSVs obtained by a series of calibrated Mass Flow Controllers (Brookhorst) was continuously fed through the catalytic bed maintained at the target temperature. Gases at the reactor outlet are passed through a trap filled with silicon carbide pellets where water is condensed before reaching the gas chromatograph. Reactants and products were analysed on-line by a CP-3800 gas chromatograph (GC) equipped with a thermal conductivity (TCD) and flame ionization (FID) detectors. All reactor exit lines were maintained at $110\text{ }^\circ\text{C}$ by external heating tapes as to avoid condensation of residual water in the feed. CO_2 conversion (X_{CO_2}) and CH_4 selectivity (S_{CH_4}) were calculated according to the following equations [Eqs. (2) and (3)]:

$$X_{\text{CO}_2} (\%) = \frac{F_{\text{CO}_2(\text{in})} - F_{\text{CO}_2(\text{out})}}{F_{\text{CO}_2(\text{in})}} \times 100 \quad (2)$$

$$S_{\text{CH}_4} (\%) = \frac{F_{\text{CH}_4(\text{out})}}{F_{\text{CH}_4(\text{out})} + F_{\text{CO}(\text{out})}} \times 100 \quad (3)$$

where F (mL min^{-1}) is the flow rate of each component in the gas feed at the reactor inlet or outlet.

Acknowledgements

G. G. and C. P.-H. thank the TRAINER project (Catalysts for Transition to Renewable Energy Future) of the "Make our Planet Great Again" program (Ref. ANR-17-MPGA-0017) for support. The Italian team would also like to thank the Italian MIUR through the PRIN 2017 Project Multi-e (20179337R7) "Multielectron transfer for the conversion of small molecules: an enabling technology for the chemical use of renewable energy" for financial support to this work. Y. L. acknowledges NSFC of China (21872144, 21972140 and 91645117) and CAS Youth Innovation Promotion Association (2018220) for support. W. W. would like to thank the China Scholarship Council (CSC) for financial support during his Ph.D. stay at the ICPEES.

Conflict of Interest

The authors declare no conflict of interest.

Keywords: CO_2 methanation · heterogeneous catalysis · induction heating · Ni-loaded $\gamma\text{-Al}_2\text{O}_3$ · sustainable chemistry

- [1] A Roadmap for moving to a competitive low carbon economy in 2050, European Commission, 2011.
- [2] J. Ma, Q. Li, M. Kühn, N. Nakaten, *Renew. Sustainable Energ. Rev.* **2018**, *97*, 478–496.
- [3] a) E. P. Ahern, P. Deane, T. Persson, B. Ó. Gallachóir, J. D. Murphy, *Renewable Energy* **2015**, *78*, 648–656; b) S. Saeidi, N. A. S. Amin, M. R. Rahimpour, *J. CO₂ Util.* **2014**, *5*, 66–81; c) H. Chen, T. N. Cong, W. Yang, C. Tan, Y. Li, Y. Ding, *Proc. Natl. Sci. USA* **2009**, *19*, 291–312.
- [4] M. Götz, J. Lefebvre, F. Mörs, A. M. Koch, F. Graf, S. Bajohr, R. R. T. Kolb, *Renewable Energy* **2016**, *85*, 1371–1390.
- [5] a) G. Centi, E. A. Quadrelli, S. Perathoner, *Energy Environ. Sci.* **2013**, *6*, 1711–1731; b) K. Hashimoto, N. Kumagai, K. Izumiya, H. Takano, Z. Kato, *Energy Sustainable Soc.* **2014**, *4*, 17; c) M. Jentsch, T. Trost, M. Sterner, *Energy Procedia* **2014**, *46*, 254–261; d) S. Rönsch, J. Schneider, S. Matthischke, M. Schlüter, M. Götz, J. Lefebvre, P. P. S. Bajohr, *Fuel* **2016**, *166*, 276–296.
- [6] a) A. Lewandowska-Bernat, U. Desideri, *Appl. Energy* **2018**, *228*, 57–67; b) W. Li, H. Wang, X. Jiang, J. Zhu, Z. Liu, X. Guo, C. Song, *RSC Adv.* **2018**, *8*, 7651–7669; c) F. D. Meylan, V. Moreau, S. Erkman, *Energy Policy* **2016**, *94*, 366–376; d) M. Bailera, P. Lisbona, L. M. Romeo, S. Espotolero, *Renewable Sustainable Energy Rev.* **2017**, *69*, 292–312.
- [7] W. Wang, S. Wang, X. Ma, J. Gong, *Chem. Soc. Rev.* **2011**, *40*, 3703–3727.
- [8] a) A. Bordet, L.-M. Lacroix, P.-F. Fazzini, J. Carrey, K. Soulantica, B. Chaudret, *Angew. Chem. Int. Ed.* **2016**, *55*, 15894–15898; *Angew. Chem.* **2016**, *128*, 16126–16130; b) W. Wang, G. Tuci, C. Duong-Viet, Y. Liu, A. Rossin, L. Luconi, J.-M. Nhut, L. Nguyen-Dinh, C. Pham-Huu, G. Giambastiani, *ACS Catal.* **2019**, *9*, 7921–7935.
- [9] a) C. Janke, M. S. Duyar, M. Hoskins, R. Farrauto, *Appl. Catal. B* **2014**, *152–153*, 184–191; b) I. Kiendl, M. Klemm, A. Clemens, A. Herrman, *Fuel* **2014**, *123*, 211–217; c) D. Schlereth, P. J. Donaubauer, O. Hinrichsen, *Chem. Eng. Technol.* **2015**, *38*, 1845–1852; d) M. C. Seemann, T. J. Schildhauer, S. M. A. Biollaz, *Ind. Eng. Chem. Res.* **2010**, *49*, 7034–7038.
- [10] A. Renken, L. Kiwi-Minsker, *Adv. Catal.* **2010**, *53*, 47–122.

- [11] Y. Li, Q. Zhang, R. Chai, G. Zhao, Y. Liu, Y. Lu, F. Cao, *AIChE J.* **2015**, *61*, 4323–4331.
- [12] a) W. Wang, C. Duong-Viet, Z. Xu, H. Ba, G. Tuci, G. Giambastiani, Y. Liu, T. Truong-Huu, J. M. Nhut, C. Pham-Huu, *Catal. Today* **2019**, DOI: 10.1016/j.cattod.2019.1002.1050; **any news?** b) W. Wang, C. Duong-Viet, H. Ba, W. Baaziz, G. Tuci, S. Caporali, L. Nguyen-Dinh, O. Ersen, G. Giambastiani, C. Pham-Huu, *ACS Appl. Energy Mater.* **2019**, *2*, 1111–1120.
- [13] a) W. Wang, W. Chu, N. Wang, W. Yang, C. Jiang, *Int. J. Hydrogen Energy* **2016**, *41*, 967–975; b) M. Frey, T. Romero, A. C. Roger, D. Edouard, *Catal. Today* **2016**, *273*, 83–90; c) L. Li, J. Zheng, Y. Liu, W. Wang, Q. Huang, W. Chu, *ChemistrySelect* **2017**, *2*, 3750–3757; d) M. Frey, A. Bengaouer, G. Geffraye, D. Edouard, A.-C. Roger, *Energy Technol.* **2017**, *5*, 2078–2085.
- [14] O. Lucia, P. Maussion, E. J. Dede, J. M. Burdío, *IEEE T. Ind. Electron.* **2013**, *61*, 2509–2520.
- [15] a) D. De Masi, J. M. Asensio, P.-F. Fazzini, L.-M. Lacroix, B. Chaudret, *Angew. Chem. Int. Ed.* **2020**, *59*, 6187–6191; *Angew. Chem.* **2020**, *132*, 6246–6250; b) B. Rivas-Murias, J. M. Asensio, N. Mille, B. Rodríguez-González, P.-F. Fazzini, J. Carrey, B. Chaudret, V. Salgueiriño, *Angew. Chem. Int. Ed.* **2020**, *59*, 15537–15542; *Angew. Chem.* **2020**, *132*, 15667–15672; **reference updated, ok?**
- [16] J. Fernández, M. Sotenko, V. Derevschikov, A. Lysikov, E. V. Rebrov, *Chem. Eng. Process.* **2016**, *108*, 17–26.
- [17] S. Chatterjee, V. Degimenci, E. V. Rebrov, *Chem. Eng. J.* **2015**, *281*, 884–891.
- [18] a) J. Gao, Q. Liu, F. Gu, B. Liu, Z. Zhong, F. Su, *RSC Adv.* **2015**, *5*, 22759–22776; b) M. A. A. Aziz, A. A. Jalil, S. Triwahyono, A. Ahmad, *Green Chem.* **2015**, *17*, 2647–2663; c) G. A. Mills, F. W. Steffgen, *Catal. Rev.* **1974**, *8*, 159–210; d) P. Frontera, A. Macario, A. Ferraro, P. Antonucci, *Catalysts* **2017**, *7*, 59; e) S. Abate, K. Barbera, E. Giglio, F. Deorsola, S. Bensaid, S. Perathoner, R. Pirone, G. Centi, *Ind. Eng. Chem. Res.* **2016**, *55*, 8299–8308; f) S. Abate, C. Mebrahtu, E. Giglio, F. Deorsola, S. Bensaid, S. Perathoner, R. Pirone, G. Centi, *Ind. Eng. Chem. Res.* **2016**, *55*, 4451–4460; g) C. Mebrahtu, S. Abate, S. Perathoner, S. Chen, G. Centi, *Catal. Today* **2018**, *304*, 181–189; h) C. Mebrahtu, F. Krebs, S. Perathoner, S. Abate, G. Centi, R. Palkovits, *Catal. Sci. Technol.* **2018**, *8*, 1016–1027.
- [19] a) T. Wang, H. Ma, L. Zeng, D. Li, H. Tian, S. Xiao, J. Gong, *Nanoscale* **2016**, *8*, 10177–10187; b) C. Mebrahtu, S. Perathoner, G. Giorgianni, S. Chen, G. Centi, F. Krebs, R. Palkovits, S. Abate, *Catal. Sci. Technol.* **2019**, *9*, 4023–4035.
- [20] D. Beierlein, D. Häussermann, M. Pfeifer, T. Schwarz, K. Stöwe, Y. Traa, E. Klemm, *Appl. Catal. B* **2019**, *247*, 200–219.
- [21] B. Lu, K. Kawamoto, *Fuel* **2013**, *103*, 699–704.
- [22] The mean Ni particle size from H₂ chemisorption was in excellent accord with the average values estimated via XRD analyses from full-width half-maximum (FWHM) values of the diffraction peaks at $2\theta = 51.8^\circ$. Indeed, for the two most representative samples of this series ³⁰Ni/ γ -Al₂O₃ and ⁴⁰Ni/ γ -Al₂O₃ the calculated mean particle size from XRD spectra were 15.6 and 18.5 nm, respectively
- [23] For a standardized procedure see on “Datasheet & Manuals” at the following link: <https://www.optris.global/optris-claser-lt> (accessed Feb, 2020)
- [24] J. Carrey, B. Mehdaoui, M. Respaud, *J. Appl. Phys.* **2011**, *109*, 083921.
- [25] C. Appino, O. De La Barrière, F. Fiorillo, M. Lobue, F. Mazaleyrat, C. Ragusa, *J. Appl. Phys.* **2013**, *113*, 17 A322–321–317 A322–323.
- [26] J. M. D. Coey, *Magnetism and Magnetic Materials*, Cambridge University Press, New York, **2010**
- [27] S. Ruta, R. Chantrell, O. Hovorka, *Sci. Rep.* **2015**, *5*, 9090.
- [28] a) A. Riedinger, P. Guardia, A. Curcio, M. A. Garcia, R. Cingolani, L. Manna, T. Pellegrino, *Nano Lett.* **2013**, *13*, 2399–2406; b) A. Meffre, B. Mehdaoui, V. Connord, J. Carrey, P. F. Fazzini, S. Lachaize, M. Respaud, B. Chaudret, *Nano Lett.* **2015**, *15*, 3241–3248; c) T. Hartman, R. G. Geitenbeek, G. T. Whiting, B. M. Weckhuysen, *Nat. Can.* **2019**, *2*, 986–996.
- [29] C. Niether, S. Faure, A. Bordet, J. Deseure, M. Chatenet, J. Carrey, C. B. A. Rouet, *Nat. Energy* **2018**, *3*, 476–483.
- [30] a) J. Corcoran, P. B. Nagy, *J. Nondestruct. Eval.* **2016**, *35*, 58; b) A. Skumiel, M. Kaczmarek-Klinowska, M. Timko, M. Molcan, M. Rajnak, *Int. J. Thermophys.* **2013**, *34*, 655–666.
- [31] M. D. Argyle, C. H. Bartholomew, *Catalysts* **2015**, *5*, 145–269.
- [32] S. Ma, Y. Tan, Y. Han, *J. Nat. Gas Chem.* **2011**, *20*, 435–440.
- [33] a) J. Zhang, W. Guo, Q. Li, Z. Wang, S. Liu, *Environ. Sci. Technol.* **2018**, *5*, 2482–2499; b) N. Wilson, *BioScience* **2018**, *68*, 241–246.
- [34] J. Gao, Y. Wang, Y. Ping, D. Hu, G. Xu, F. Gu, F. Su, *RSC Adv.* **2012**, *2*, 2358–2368.
- [35] a) D. Lupu, A. R. Biris, A. Jianu, C. Bunesco, E. Burkel, E. Indrea, G. Mihailescu, S. Pruneanu, L. Olenic, I. Misan, *Carbon* **2004**, *42*, 503–507; b) S. Ramakrishnan, E. J. Jelmy, M. Dhakshnamoorthy, M. Rangarajan, N. Kothurkar, *Synth. React. Inorg.* **2014**, *44*, 873–876.
- [36] T. A. Le, M. S. Kim, S. H. Lee, T. W. Kim, E. D. Park, *Catal. Today* **2017**, *293*, 89–96.
- [37] J. Lin, C. Ma, Q. Wang, Y. Xu, G. Ma, J. Wang, H. Wang, C. Dong, C. Zhang, M. Ding, *Appl. Catal. B* **2019**, *243*, 262–272.
- [38] G. Garbarino, C. Wang, T. Cavattoni, E. Finocchio, P. Riani, M. Flytzani-Stephanopoulos, G. Busca, *Appl. Catal. B* **2019**, *248*, 286–297.
- [39] J. Sun, Y. Wang, H. Zou, X. Guo, Z. J. Wang, *J. Energy Chem.* **2019**, *29*, 3–7.
- [40] A. Quindimil, U. De-La-Torre, B. Pereda-Ayo, A. Davó-Quiñonero, E. Bailón-García, D. Lozano-Castelló, J. A. González-Marcos, A. Bueno-López, J. R. González-Velasco, *Catal. Today* **2019**, *in press*.
- [41] S. He, C. Li, H. Chen, D. Su, B. Zhang, X. Cao, B. Wang, M. Wei, D. G. Evans, X. Duan, *Chem. Mater.* **2013**, *25*, 1040–1046.
- [42] B. Mutz, M. Belimov, W. Wang, P. Sprenger, M.-A. Serrer, D. Wang, P. Pfeifer, W. Kleist, J.-D. Grunwaldt, *ACS Catal.* **2017**, *7*, 6802–6814.
- [43] L. Xu, F. Wang, M. Chen, D. Nie, X. Lian, Z. Lu, H. Chen, K. Zhang, P. Ge, *Int. J. Hydrogen Energy* **2017**, *42*, 15523–15539.
- [44] L. He, Q. Lin, Y. Liu, Y. Huang, *J. Energy Chem.* **2014**, *23*, 587–592.
- [45] K. Stangeland, D. Y. Kalai, H. Li, Z. Yu, *Appl. Energy* **2018**, *227*, 206–212.
- [46] B. Mutz, A. M. Gänzler, M. Nachttegaal, O. Müller, R. Frahm, W. Kleist, J.-D. Grunwaldt, *Catalysts* **2017**, *7*, 279.
- [47] X. Guo, Z. Peng, M. Hu, C. Zuo, A. Traitangwong, V. Meeyoo, C. Li, S. Zhang, *Ind. Eng. Chem. Res.* **2018**, *57*, 9102–9111.
- [48] G. Garbarino, P. Riani, L. Magistri, G. Busca, *Int. J. Hydrogen Energy* **2014**, *39*, 11557–11565.
- [49] M. Cai, J. Wen, W. Chu, X. Cheng, Z. Li, *J. Nat. Gas Chem.* **2011**, *20*, 318–324.
- [50] H. Liu, X. Zou, X. Wang, X. Lu, W. Ding, *J. Nat. Gas Chem.* **2012**, *21*, 703–707.
- [51] S. Rahmani, M. Rezaei, F. Meshkani, *J. Ind. Eng. Chem.* **2014**, *20*, 1346–1352.
- [52] S. Rahmani, M. Rezaei, F. Meshkani, *J. Ind. Eng. Chem.* **2014**, *20*, 4176–4182.
- [53] S. Danaci, L. Protasova, J. Lefevère, L. Bedel, R. Guilet, P. Marty, *Catal. Today* **2016**, *273*, 234–243.
- [54] R. Daroughegi, F. Meshkani, M. Rezaei, *Int. J. Hydrogen Energy* **2017**, *42*, 15115–15125.
- [55] L. Xu, X. Lian, M. Chen, Y. Cui, F. Wang, W. Li, B. Huang, *Int. J. Hydrogen Energy* **2018**, *43*, 17172–17184.
- [56] B. Alrafi, A. Polaert, A. Ledoux, F. Azzolina-Jury, *Catal. Today* **2020**, *346*, 23–33.
- [57] The catalyst pad volume for 30 and 40 wt% Ni/ γ -Al₂O₃ composites was nearly identical each other and it was fixed equal to 0.452 cm³. It was calculated assuming a catalyst pad height of 4 mm in a tubular quartz reactor of 12 mm of internal diameter.

Manuscript received: August 5, 2020

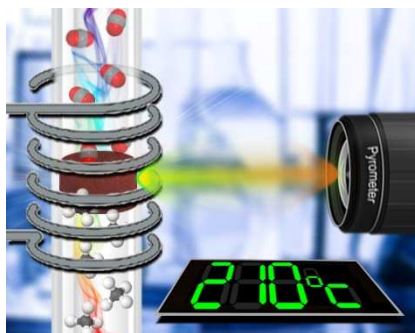
Revised manuscript received: August 28, 2020

Accepted manuscript online: September 1, 2020

Version of record online: **■■■**

FULL PAPERS

Multifunction composites: We propose a low-temperature radiofrequency-heated CO₂ methanation scheme based on Ni/ γ -Al₂O₃ composites, featuring a relatively high nickel content. These composites act as electrically conductive/magnetic susceptors for the induction heating technology while serving as robust catalysts for low-temperature CO₂ methanation. ■■■ok?■■■



Dr. W. Wang, Dr. C. Duong-Viet, Dr. G. Tuci, Prof. Y. Liu, Dr. A. Rossin, Dr. L. Luconi, Dr. J.-M. Nhut, Prof. L. Nguyen-Dinh, Dr. G. Giambastiani*, Dr. C. Pham-Huu**

1 – 12

Nickel-Loaded γ -Alumina Composites for a Radiofrequency-Heated, Low-Temperature CO₂ Methanation Scheme



 @icpees @CNRS

Share your work on social media! *ChemSusChem* has added Twitter as a means to promote your article. Twitter is an online microblogging service that enables its users to send and read short messages and media, known as tweets. Please check the pre-written tweet in the galley proofs for accuracy. If you, your team, or institution have a Twitter account, please include its handle @username. Please use hashtags only for the most important keywords, such as #catalysis, #nanoparticles, or #proteindesign. The ToC picture and a link to your article will be added automatically, so the **tweet text must not exceed 250 characters**. This tweet will be posted on the journal's Twitter account (follow us @ChemSusChem) upon publication of your article in its final (possibly unpaginated) form. We recommend you to re-tweet it to alert more researchers about your publication, or to point it out to your institution's social media team.

ORCID (Open Researcher and Contributor ID)

Please check that the ORCID identifiers listed below are correct. We encourage all authors to provide an ORCID identifier for each coauthor. ORCID is a registry that provides researchers with a unique digital identifier. Some funding agencies recommend or even require the inclusion of ORCID IDs in all published articles, and authors should consult their funding agency guidelines for details. Registration is easy and free; for further information, see <http://orcid.org/>.

Dr. Wei Wang
Dr. Cuong Duong-Viet
Dr. Giulia Tuci
Prof. Yuefeng Liu
Dr. Andrea Rossin
Dr. Lapo Luconi
Dr. Jean-Mario Nhut
Prof. Lam Nguyen-Dinh
Dr. Giuliano Giambastiani <http://orcid.org/0000-0002-0315-3286>
Dr. Cuong Pham-Huu